

Early Paleozoic slab rollback in the North Altun, Northwest China: New evidence from mafic intrusions and high-Mg andesites

Xian-Tao Ye¹, Chuan-Lin Zhang¹, Ai-Guo Wang², Bin Wu², and Guo-Dong Wang³

¹China University of Geosciences, Beijing, 100083, China

²State Key Laboratory of Geological Processes and Mineral Resources, Beijing, 100083, China

³State Key Laboratory of Geological Processes and Mineral Resources, Beijing, 100083, China

ABSTRACT

The North Altun orogen in Northwest China is a tectonically complex area. The Early Paleozoic tectonic evolution of this area is still controversial. In this study, we report new evidence from mafic intrusions and high-Mg andesites. The mafic intrusions are composed of dioritic and andesitic dykes, which are dated to 480–520 Ma by ⁴⁰Ar/³⁹Ar dating. The high-Mg andesites are characterized by high MgO content (10–12 wt%), low TiO₂ content (0.5–1.0 wt%), and high Mg# (0.6–0.7). These features suggest that the mafic rocks were formed in a subduction-related setting. The mafic rocks are associated with a high-Mg andesite, which is a typical feature of a slab rollback setting. The mafic rocks and high-Mg andesite provide new evidence for the Early Paleozoic slab rollback in the North Altun orogen. The mafic rocks and high-Mg andesite are dated to 480–520 Ma, which is consistent with the presence of arc-related granitic rocks and the occurrence of early Paleozoic ophiolites in the belt. The mafic rocks and high-Mg andesite provide new evidence for the Early Paleozoic slab rollback in the North Altun orogen.

10.1016/j.tecto.2018.07.010; Received 10 July 2018; Accepted 10 July 2018; Available online 10 July 2018

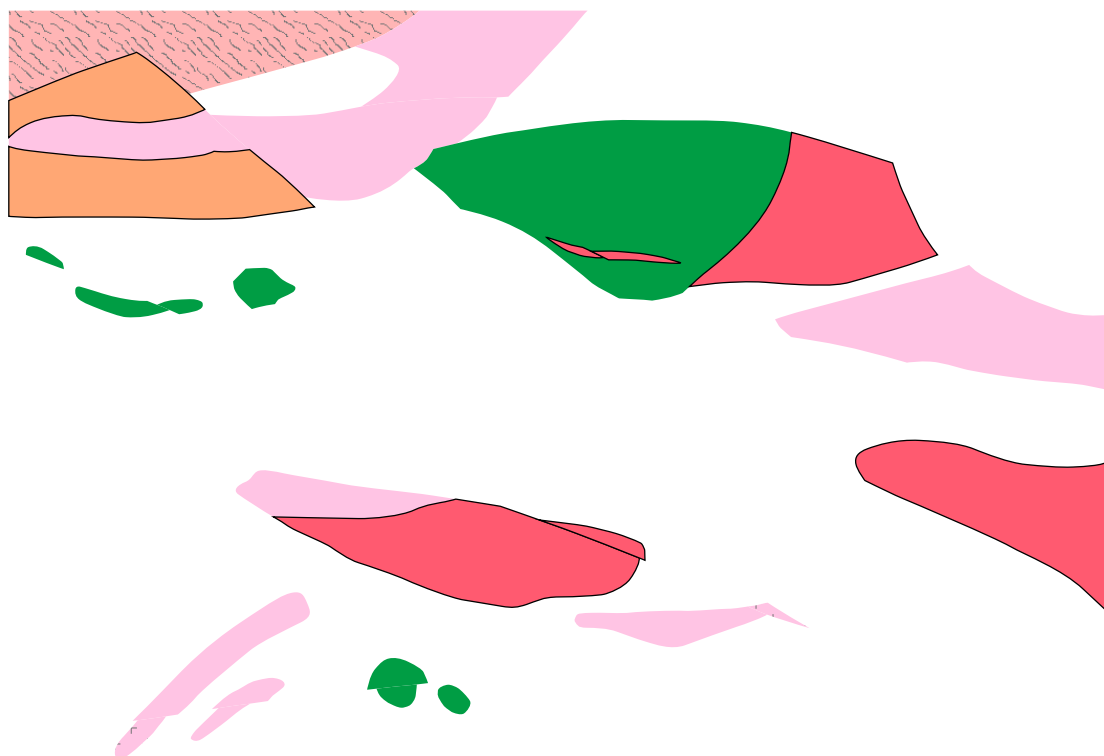
INTRODUCTION

The Altun orogen is located at the northern margin of the Qinhai-Tibet Plateau (Fig. 1A; Wu et al., 2006, 2009; Xu et al., 1999, 2011). Recent studies show that the Altun orogen is a composite orogenic belt, consisting of microcontinents and multiple ophiolite and high-pressure to ultrahigh-pressure metamorphic belts (Xu et al., 1999; Zhang et al., 2005b). In spite of many studies in the area, its Paleozoic tectonic evolution has remained equivocal (Cowgill et al., 2003; L. Liu et al., 1997, 2007; Sobel and Arnaud, 1999; Wu et al., 2006, 2016; J.X. Zhang et al., 2005a, 2005b; Z.C. Zhang et al., 2010b).

Based on the age of the high-pressure and low-temperature (HP/LT) metamorphic rocks in the North Altun, Zhang et al. (2007) suggested that slab subduction began ca. 520 Ma. This is consistent with the presence of arc-related granitic rocks and the occurrence of early Paleozoic ophiolites

in the belt (Gai et al., 2015; Gao et al., 2012; Yang et al., 2008). However, the tectonic evolution of this area was divided into different stages by previous scholars (e.g., Han et al., 2012; Liu et al., 2016; Meng et al., 2017). In addition, the early Paleozoic tectonic evolution, especially the subduction history of the belt, has not yet been characterized (Meng et al., 2017).

Mafic rocks are known to occur in the North Altun (Xinjiang BGMR, 1981, 2006), but little is known about their geochronology or petrogenesis or their relationship with the widespread silicic magmatism. Mafic rocks have different geochemical features that result from the different tectonic settings in which they formed. These features can also be used to constrain the nature of the mantle source (Hollanda et al., 2006; Yang and Zhou, 2009), the extent of metasomatism by subduction-related materials (Kepezhinskis et al., 1997), and the degree of interaction between mantle-derived magmas and crustal materials (DePaolo, 1981). Therefore,



eclogites formed during 510–490 Ma (Zhang and Meng, 2006; J.X. Zhang et al., 2005b, 2007, 2010). Granitoids can be subdivided into two groups: 520–470 Ma subduction-related I-type granites (Han et al., 2012; Kang et al., 2011; C. Liu et al., 2016; J.H. Liu et al., 2017; Wu et al., 2006) and 440–410 Ma I- and S-type anorogenic granites (Chen et al., 2003, 2009; Han et al., 2012; Z.C. Zhang et al., 2010b). Based on the presence of HP/LT metamorphic assemblages, and ophiolitic, subduction-accretion complex, and arc magmatic rocks, Zhang et al. (2015) proposed that the North Altun could be considered as a typical early Paleozoic accretionary orogenic belt.

Compared to the extensive distribution of granitoids along the North Altun, rare gabbroic intrusions occurred in this area. These intrusions form an E–W–trending belt from Hongliugou to Lapeiquan (Fig. 1C). The Katalawan area, located in the eastern North Altun, hosts the Lapeiquan Formation, granitoids, and several mafic intrusions (Dawan and Dabanxi intrusions) and the Dawan mafic dikes. However, the emplacement ages, petrogenesis, and tectonic regime of these mafic rocks remain unknown.

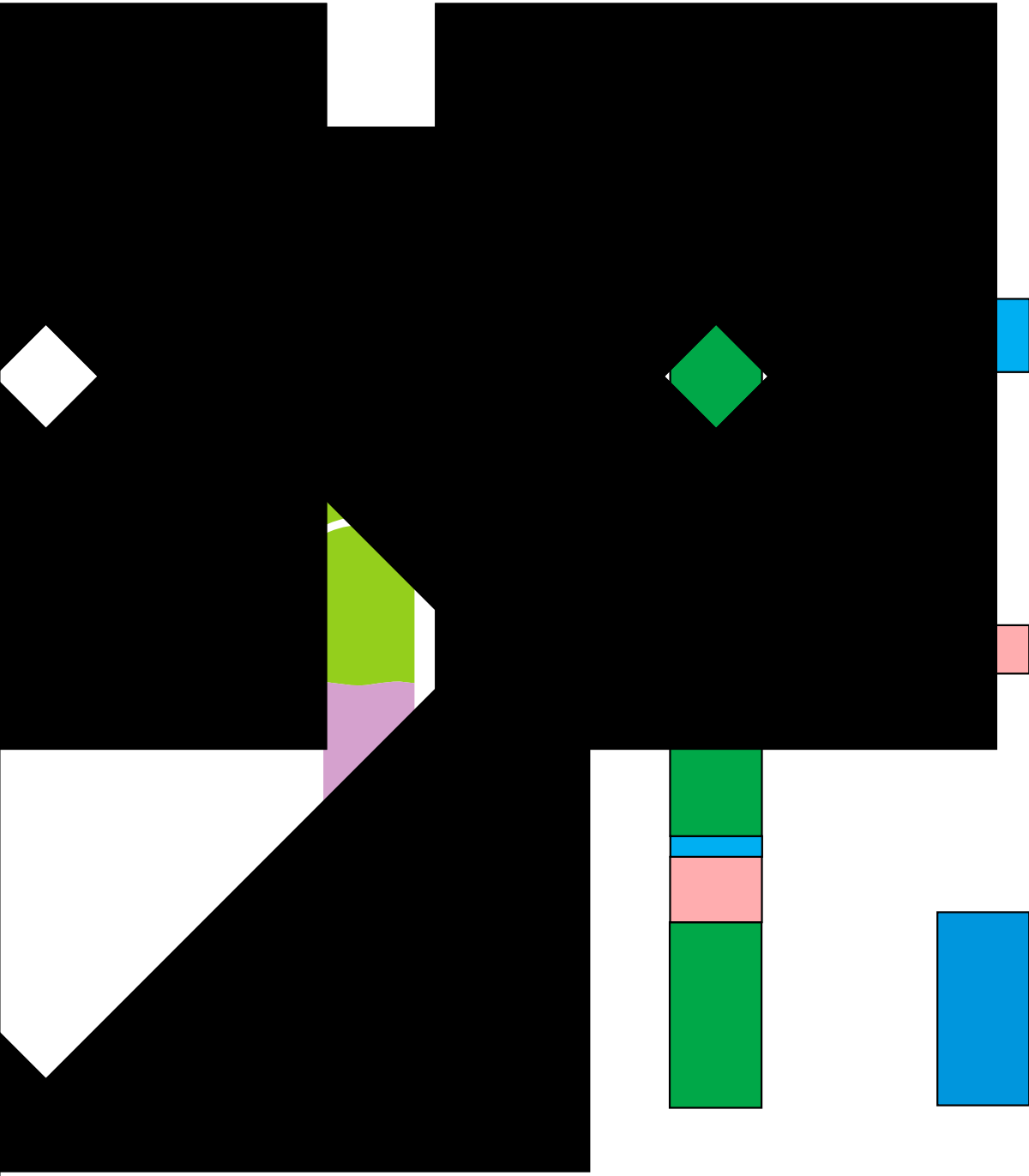
FIELD OBSERVATION AND SAMPLE COLLECTION

Lapeiquan Formation

The Lapeiquan Formation is divided into lower and upper sections, outcropping along the Hongliugou–Lapeiquan ophiolite belt (Figs. 2 and 3A).

The Lapeiquan Formation unconformably overlies the Neoproterozoic Muzisayi Formation. At its southern margin, it connects with the Paleogene Gancaigou Formation by a thrust fault. The lower section of the Lapeiquan Formation consists mainly of layers of mafic to silicic volcanic and volcaniclastic rocks, including basalt, andesite, dacite, rhyolite, and sericite-chlorite (quartz) schist (Fig. 3B; Ni et al., 2017; Xinjiang BGMR, 2006). In addition, it hosts a massive iron-ore deposit (Qi et al., 2008). The upper section of the Lapeiquan Formation is composed chiefly of clastic rocks, interbedded with minor metavolcanics and carbonates (Fig. 3C). It underwent lower-greenschist-facies metamorphism and tightly folded deformation. The upper Lapeiquan Formation sedimentary sequence extends more than 100 km from Qiongtage to the Lapeiquan area. Field and thin section observations have revealed that the major rock types are sericite-chlorite (quartz) schist, fine-grained sandstone, rhyolite, phyllite, ignimbrite, and dolomite. Lower-greenschist-facies metamorphic minerals such as biotite, sericite, and chlorite are commonly seen in most rock types. It should be noted that the upper Lapeiquan Formation hosts a large Pb–Zn–Ag–Cu polymetallic ore deposit in this region.

One rhyolite sample from the lower Lapeiquan Formation (16AB02: 39°07′14″N, 91°37′51″E; Fig. 4A) and two rhyolite samples from the upper Lapeiquan Formation (1101: 39°03′40″N, 91°37′51″E and 1106: 39°07′14″N, 91°37′51″E; Fig. 4B) were collected for zircon U–Pb dating. Ten andesitic samples (39°05′22″N, 91°44′55″E) were collected for



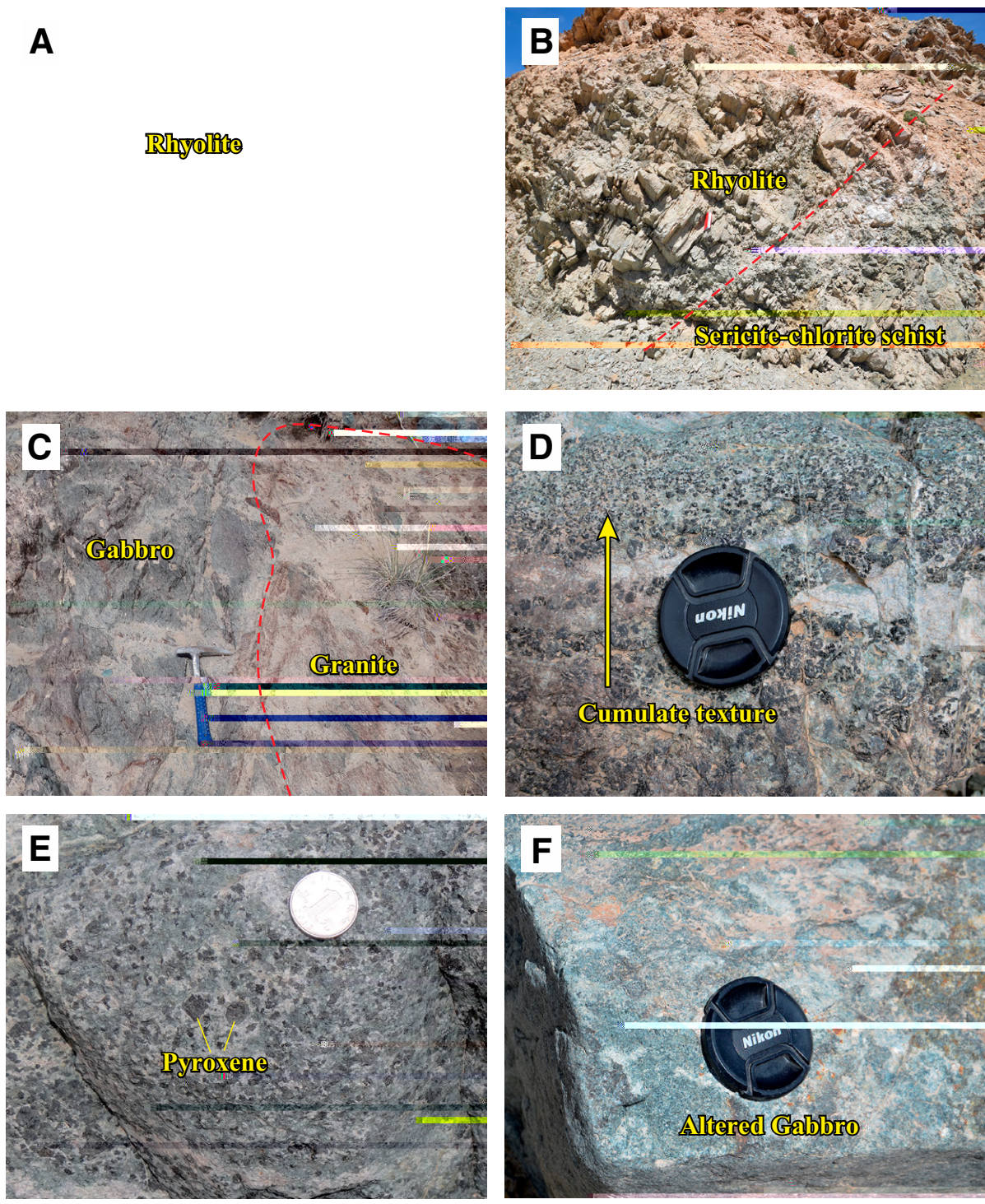


Figure 4. Field photographs of the Dawan mafic intrusion, rhyolite from the lower and upper Lapeiquan Formation, and the Dabanxi mafic intrusion: (A) cumulate structure of the Dawan gabbros; (B) euhedral pyroxenes in the Dawan gabbros; (C) intrusive contact between the Dawan mafic intrusion and granitic rocks; (D) interbedded rhyolite layer from the lower Lapeiquan Formation; (E) relationship between the rhyolite and sericite-chlorite schist from the upper Lapeiquan Formation; and (F) alteration of gabbro from the Dabanxi mafic intrusion.

geochemical work. Rhyolites have euhedral to subhedral crystal plagioclase and potassium feldspar (K-feldspar; Figs. 5A and 5B), whereas andesites contain plagioclase (30%–45%), hornblende (40%–45%), K-feldspar (5%–10%), quartz (5%–10%), and minor epidote, zircon, and apatite (Fig. 5C).

Dawan Intrusion

The Dawan gabbroic intrusion is one of the largest mafic intrusions in the Kaladawan area. It shares a fault contact with country rocks (Xinjiang BGMR, 2006), and then is intruded by a granitic pluton (Fig. 4C). Massive structure and cumulate texture are evident. Rhythmic layering of plagioclase and pyroxene is commonly observed at several outcrops in the field (Fig. 4D). The gabbro has typical gabbroic texture with euhedral to semi-euhedral pyroxene and plagioclase in both outcrop and thin sections (Figs. 4E, 5D, and 5E). The main minerals are clinopyroxene (40%–50%) and plagioclase (30%–45%). The minor minerals include hornblende

and epidote. Zircon, titanite, and apatite are present as accessory minerals. One geochronological sample (16DW02: 39°08′08″N, 91°43′19″E) and seven geochemical samples were collected from this pluton. In addition, one sample from the granitic pluton intruding the gabbro (AYT001: 39°08′31″N, 91°42′5″E) was collected for geochronological analysis.

Dabanxi Intrusion

In the Kaladawan area, dozens of E-W-trending mafic intrusions and dikes were emplaced in the lower Lapeiquan Formation (Fig. 2). Among them, the Dabanxi intrusion, of coarse-grained texture and with a total outcrop area of ~1 km², is relatively suitable for zircon selection.

The dominant rocks of the Dabanxi stocks are coarse- to medium-grained gabbros (Fig. 4F). The gabbros are generally composed of euhedral crystals of plagioclase and clinopyroxene, with minor hornblende, biotite, apatite, and Fe-Ti oxides. Most of the gabbros have experienced

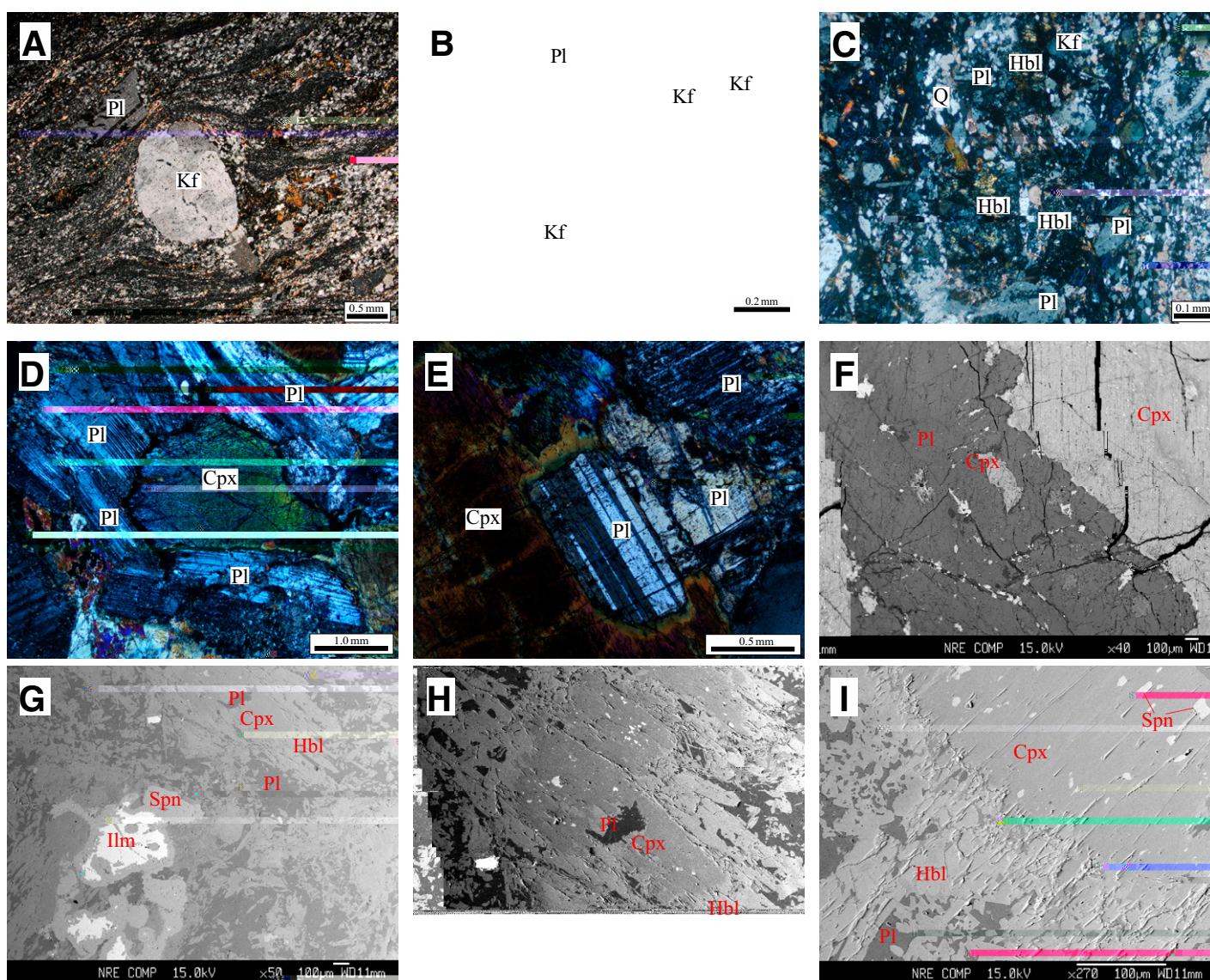


Figure 5. Photomicrographs of: (A, B, C) Dawan gabbros, (D) rhyolite from the lower Lapeiquan Formation, (E) rhyolite from the upper Lapeiquan Formation, (F) andesite from the lower Lapeiquan Formation, and (G, H, I) Dabanxi gabbros (see details in the text). Cpx—clinopyroxene; Hbl—hornblende; Ilm—ilmenite; Kf—K-feldspar; Pl—plagioclase; Q—quartz; Spn—spinel.

variable degrees of alteration, resulting in albitization of some plagioclases and some alteration of clinopyroxene to amphibole, chlorite, or epidote (Fig. 5G). In thin section, the gabbro contains 40%–50% plagioclase and 45%–50% clinopyroxene, with minor hornblende, epidote, sphene, and Fe-Ti oxides (Figs. 5H and 5I). One sample for geochronology (16DBX04: 39°04'19"N, 91°41'55"E) and 10 samples for geochemical analyses were collected from this intrusion.

ANALYTICAL METHODS

Zircon separation was carried out using conventional heavy liquid and magnetic separation techniques. Zircon grains were then handpicked under a binocular microscope, and representative grains and zircon standards (TEMORA) were mounted in epoxy resin disks. These were then polished to approximately half their thickness. Zircons were photographed under transmitted and reflected light, and cathodoluminescence (CL) images were taken to reveal their internal structures.

Zircon U-Pb analyses were carried out using sensitive high-resolution ion microprobe II (SHRIMP II) and laser ablation-inductively coupled plasma-mass spectrometry (LA-ICP-MS) techniques at the Beijing SHRIMP Center, Chinese Academy of Geological Sciences, and Tianjin Institute of Geology and Mineral Resources, respectively. Ion microprobe procedures followed those described by Williams (1998), whereas LA-ICP-MS analytical procedures were described by Geng et al. (2011) and Hou et al. (2009). Data reduction was performed off-line using ICPMS-DataCal (Liu et al., 2010a, 2010b). SQUID 1.0 and Isoplot (Ludwig, 1999) software were used for data processing. Zircon U-Pb age data are listed in Table DR1 in the GSA Data Repository Item.¹

Clinopyroxene compositions were determined by wavelength-dispersion X-ray emission spectrometry using a JEOL JXA-8100 electron-probe microanalyzer (EMPA) at the State Key Laboratory Breeding Base of Nuclear Resources and Environment, Nanchang, China. Operating conditions were 15 kV accelerating voltage and 20 nA beam current, with a 10 s counting time. Representative mineralogical data are listed in Tables DR2 and DR3 in the GSA Data Repository Item.

Major elements were measured by using a Rigaku ZSX100e X-ray fluorescence spectrometer (XRF) at the State Key Laboratory of Ore Deposit Geochemistry, Institute of Geochemistry, Chinese Academy of Sciences (CAS). Whole-rock samples were crushed and powdered to less than 200 mesh in an agate mill, and then samples were fused with lithium-tetraborate glass pellets. Analytical precision as determined by Chinese National Standards GSR-1 and GSR-3 was generally ~1%–5%. Trace elements were analyzed using a Perkin-Elmer ELAN-DRC-e ICP-MS at the State Key Laboratory of Ore Deposit Geochemistry, Institute of Geochemistry, CAS. Powdered samples (50 mg) were digested in high-pressure Teflon bombs using an HF + HNO₃ mixture for 48 h at ~195 °C (Qi et al., 2000). Analytical precision for most elements was better than 3%–5%. Analytical results are presented in Table 1.

Samples for Nd-Sr isotopic measurement were spiked and dissolved in Teflon bombs with HF + HNO₃ acid and then separated by conventional cation-exchange techniques. The isotopic measurements were performed on a Thermo Fisher Triton TI thermal ionization mass spectrometer (TIMS) at the State Key Laboratory of Ore Deposit Geochemistry, Institute of Geochemistry, CAS. The detailed procedure we used is as described by Li et al. (2004). Measured ⁸⁷Sr/⁸⁶Sr and ¹⁴³Nd/¹⁴⁴Nd ratios were corrected to ⁸⁶Sr/⁸⁸Sr = 0.1194 and ¹⁴⁶Nd/¹⁴⁴Nd = 0.7219, respectively. The reported

⁸⁷Sr/⁸⁶Sr average ratios for the NBS987 standard and BCR-2 standard were ⁸⁷Sr/⁸⁶Sr = 0.710219 ± 5 (2σ) and 0.704966 ± 3 (2σ), respectively, and the ¹⁴³Nd/¹⁴⁴Nd average ratios for the LRIG and BCR-2 standards were ¹⁴³Nd/¹⁴⁴Nd = 0.512196 ± 3 (2σ) and 0.512634 ± 4 (2σ), respectively. Analytical results and calculated parameters are listed in Table 2.

ANALYTICAL RESULTS

Zircon U-Pb Ages

Dawan Intrusion (Gabbroic Sample 16DW02 and Granitic Sample AYT001)

Zircons in sample 16DW02 are euhedral, with average crystals size up to 50–80 μm and length-to-width ratios from 1:1 to 2:1. All zircons are colorless and without obvious zoning (Fig. 6). Fifteen grains were analyzed in this sample. Among them, five spots yielded younger ages, ranging from 222 to 406 Ma, which may reflect the effects of alteration and/or metamorphic events after emplacement, due to the absence of clear oscillatory growth zoning and presence of white or dark areas in their CL images. The other 10 spots have U and Th contents of 338–2989 ppm and 178–1678 ppm, respectively, with Th/U ratios varying from 0.11 to 0.91 (Table DR1). Most zircons show variable discordance between ²⁰⁶Pb/²³⁸U and ²⁰⁷Pb/²³⁵U ages but yield a discordance line with an intercept age of 524 ± 22 Ma (mean square of weighted deviates [MSWD] = 0.27; Fig. 7A). On the other hand, their ²⁰⁶Pb/²³⁸U ages are consistent within error and yield a weighted mean age of 515 ± 9 Ma (Fig. 7A), which is comparable to the intercept age.

Zircons from sample AYT001 are broadly euhedral (Fig. 6), with length ranging from 80 to 100 μm, and length-to-width ratio of 2:1. Thirty-two grains were analyzed on 32 grains. The data show variable U (275–1665 ppm) and Th (76–999 ppm) contents, with Th/U ratios of 0.28–0.96 (Table DR1). Excepting spots 07, 09, and 20, the other analyses define a good discordia with upper intercept age of 510 ± 3 Ma (MSWD = 0.54), and a weighted mean ²⁰⁶Pb/²³⁸U age of 511 ± 2 Ma (MSWD = 0.53; Fig. 7B).

Lapeiquan Formation (Rhyolites 16AB02, 1101, and 1106)

Zircons in sample 16AB02 are transparent, euhedral prismatic grains with concentric zoning in CL images (Fig. 6), and they are ~80 μm in length with aspect ratios of 1:1 to 2:1. Fifteen grains were analyzed, which yielded variable U and Th contents (U = 254–525 ppm, Th = 109–345 ppm, Th/U = 0.42–0.69). All analyses were concordant within analytical errors and yielded a weighted mean ²⁰⁶Pb/²³⁸U age of 495 ± 4 Ma (MSWD = 0.45; Fig. 7C).

Zircons from samples 1101 and 1106 are transparent and pinkish in color, range from 100 to 150 μm in length, and have length-to-width ratios of 2:1 to 3:1. In CL images, interval growth zoning is clear in most of the zircon crystals, and no core-rim structure is observed (Fig. 6). In total, 32 analyses on sample 1101 showed that the concentrations of U and Th are in the ranges of 401–987 ppm and 161–445 ppm, respectively, with consistent Th/U ratios between 0.37 and 0.60 (Table DR1). The measured ²⁰⁶Pb/²³⁸U ages are in good agreement within analytical error and yield a weighted mean age of 484 ± 2 Ma (MSWD = 0.78; Fig. 7D). Sample 1106 has variable contents of U (250–2007 ppm) and Th (74–1103 ppm), with Th/U ratios of 0.30–0.85 (Table DR1). All 32 analyses form a tight cluster on a concordia plot and yield a weighted mean ²⁰⁶Pb/²³⁸U age of 488 ± 2 Ma (MSWD = 0.36; Fig. 7E).

¹ SA 2018355, 1: S (16 02, 16AB02, 16 B 04) A-C - S(A, 001, 1101, 1106) 2: C - 3: C - 2018, @

TABLE 2. Sr-Nd ISOTOPIC COMPOSITIONS OF THE MAFIC ROCKS AND ANDESITES

Sample	Rock type	Rb (ppm)	Sr (ppm)	$^{87}\text{Rb}/^{86}\text{Sr}$	$^{87}\text{Sr}/^{86}\text{Sr}$ (2 σ)	$(^{87}\text{Sr}/^{86}\text{Sr})_i$	Sm (ppm)	Nd (ppm)	$^{147}\text{Sm}/^{144}\text{Nd}$	$^{143}\text{Nd}/^{144}\text{Nd}$ (2 σ)	$(^{143}\text{Nd}/^{144}\text{Nd})_i$	$\epsilon_{\text{Nd}}(t)$
Dawan intrusion												
AYT002H1	Gabbro	14.31	179	0.2313	0.706078 (22)	0.70438	0.55	1.42	0.2342	0.513141 (18)	0.5123508	7.4
AYT002H2	Gabbro	16.74	140	0.3460	0.707840 (11)	0.70530	1.51	4.26	0.2143	0.512989 (16)	0.5122664	5.7
AYT002H5	Gabbro	2.73	205	0.0385	0.705630 (12)	0.70535	0.43	1.18	0.2198	0.513078 (14)	0.5123366	7.1
AYT002H6	Gabbro	9.27	201	0.1334	0.705600 (9)	0.70462	1.52	4.45	0.2065	0.512700 (18)	0.5120032	0.6
Dawan high-Mg andesites												
AYT004H2	Andesite	109.80	249	1.2775	0.720697 (7)	0.71169	2.39	11.1	0.1302	0.512235 (19)	0.5118131	-3.7
AYT004H6	Andesite	59.31	257	0.6685	0.719358 (11)	0.71464	3.87	16.7	0.1401	0.512156 (21)	0.5117014	-5.8
Dabanxi intrusion												
AYT006H1	Gabbro	16.29	261	0.1806	0.707051 (7)	0.70587	2.21	7.07	0.1890	0.512825 (27)	0.5122551	4.1
AYT006H6	Gabbro	15.84	248	0.1848	0.707204 (7)	0.70599	1.82	6.03	0.1825	0.512626 (24)	0.5120757	0.6
AYT006H10	Gabbro	8.22	255	0.0932	0.708039 (6)	0.70743	2.94	9.92	0.1792	0.512732 (26)	0.5121918	2.9

Note: Chondritic uniform reservoir (CHUR) values ($^{87}\text{Rb}/^{86}\text{Sr} = 0.0847$, $^{87}\text{Sr}/^{86}\text{Sr} = 0.7045$; $^{147}\text{Sm}/^{144}\text{Nd} = 0.1967$, $^{143}\text{Nd}/^{144}\text{Nd} = 0.512638$) were used for the calculation. $\lambda_{\text{Sm}} = 6.54 \times 10^{-12} \text{ yr}^{-1}$ (Lugmair and Hart, 1978). The $(^{87}\text{Sr}/^{86}\text{Sr})_i$, $(^{143}\text{Nd}/^{144}\text{Nd})_i$, and $\epsilon_{\text{Nd}}(t)$ values of samples AYT002, AYT006, and AYT004 were calculated using ages of 515 Ma, 460 Ma, and 495 Ma, respectively. The two-stage model age ($T_{2\text{DM}}$) calculations may be found in Jahn et al. (1999).

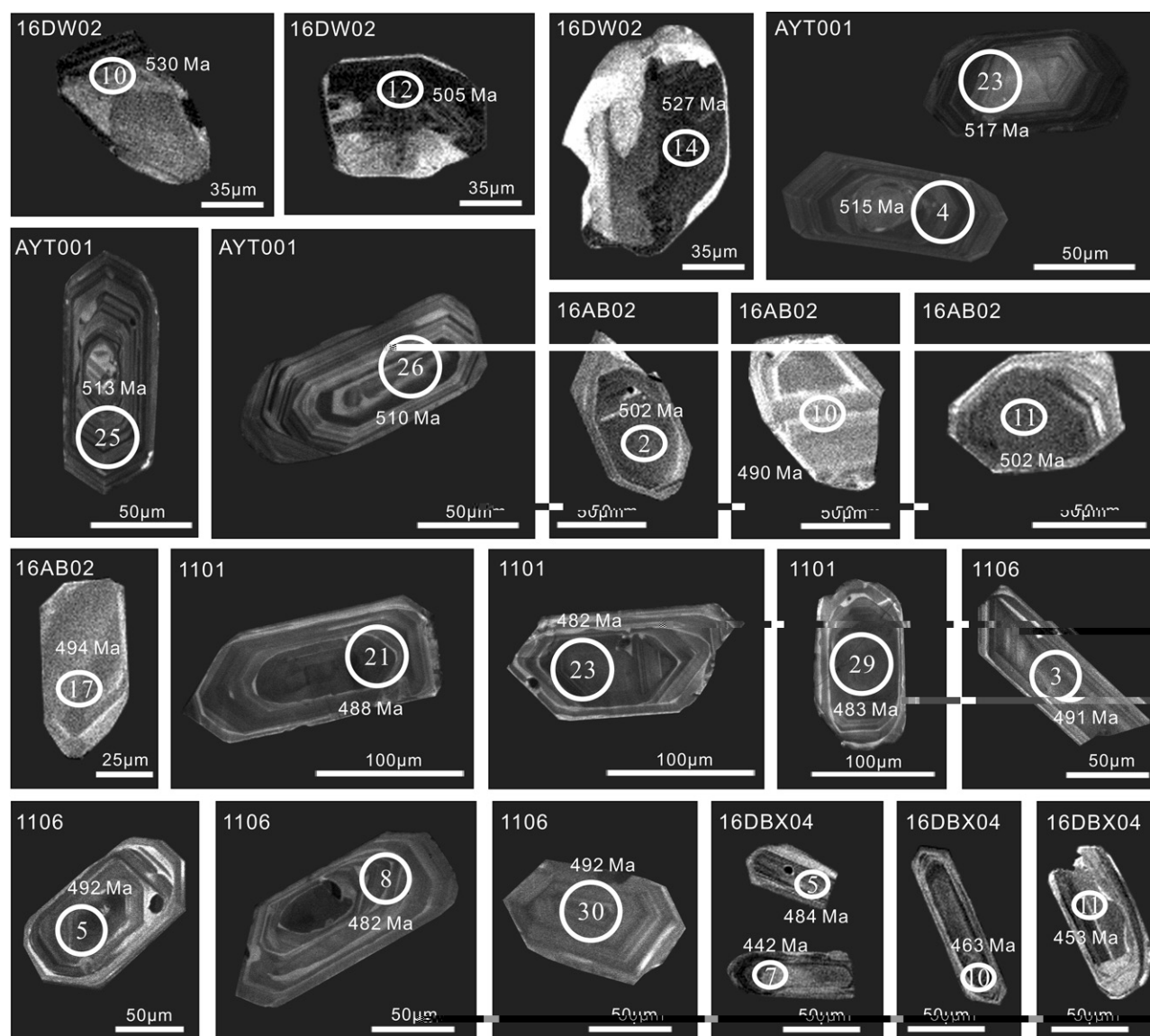
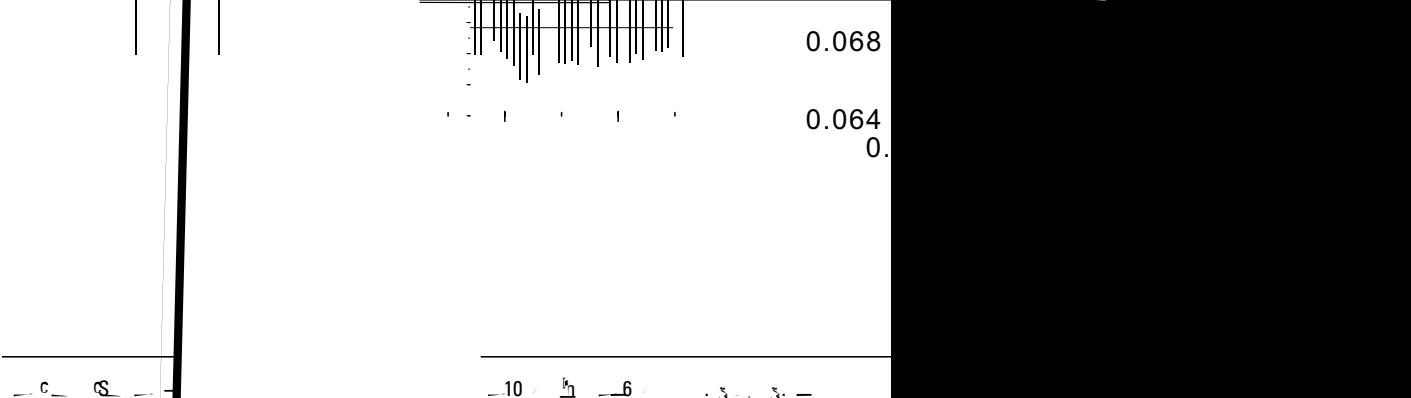
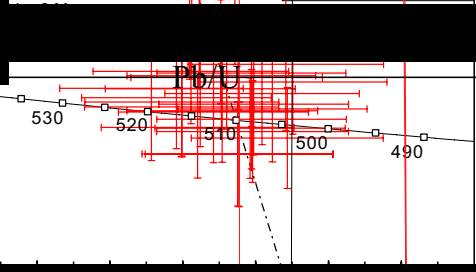
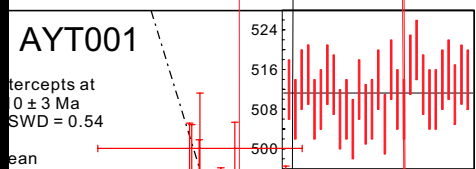
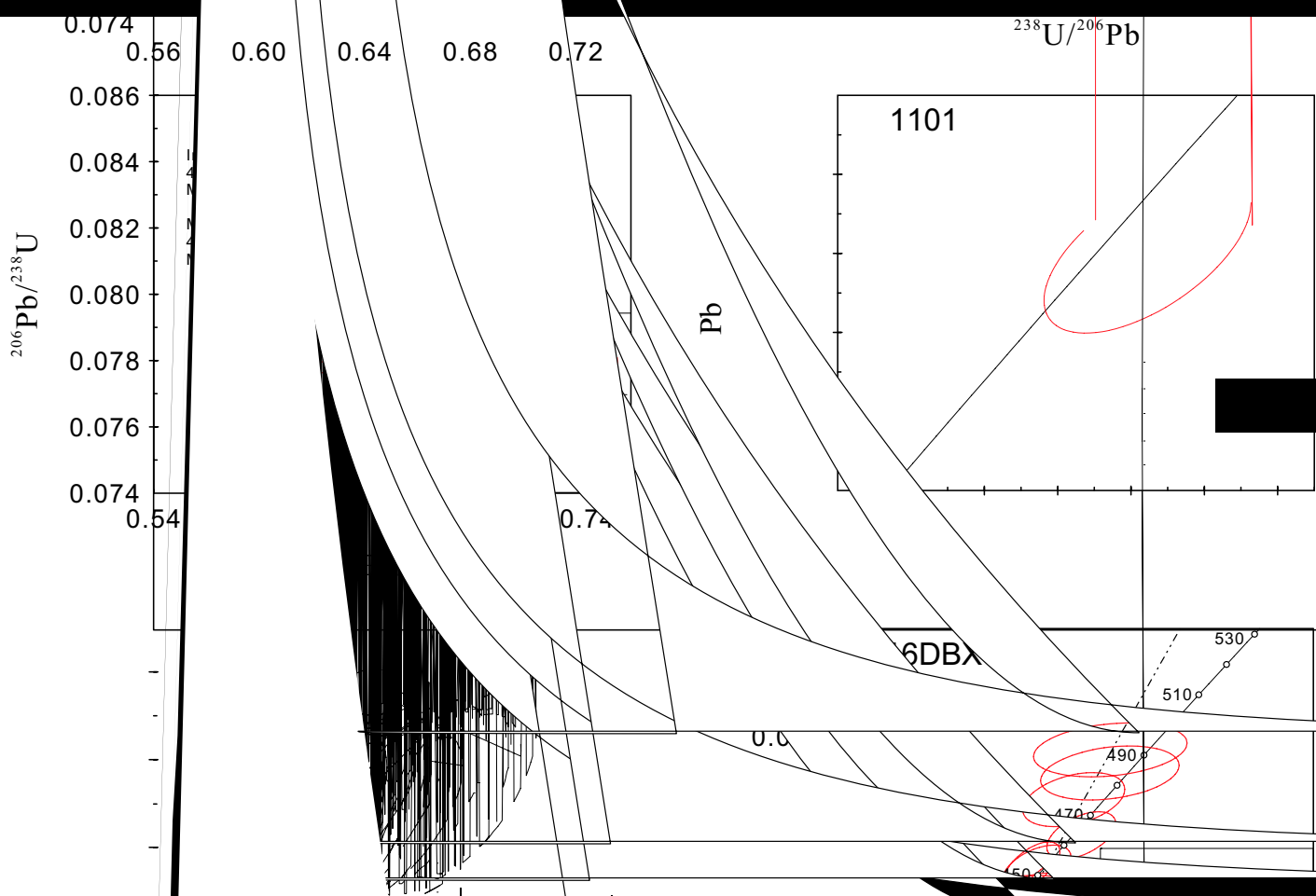
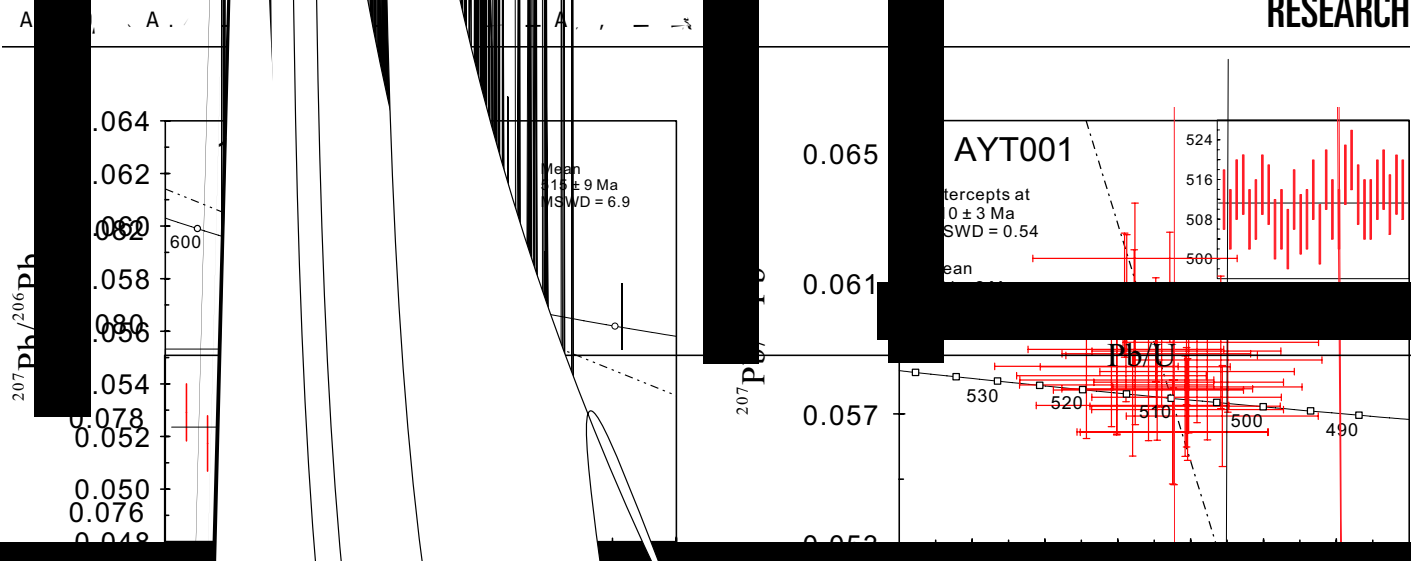


Figure 6. Representative cathodoluminescence (CL) images of zircon from the Dawan mafic intrusion, rhyolites from the lower and upper Lapeiquan Formation, and the Dabanxi mafic intrusion. Analytical spots and ages are shown (see details in the text).



Dabanxi Intrusion (Gabbroic Sample 16DBX04)

Zircons from sample 16DBX04 are transparent and are 50–150 μm in length, with length-to-width ratios between 1:1 and 3:1. Most zircons are prismatic crystals without obvious zoning in CL images (Fig. 6). Fifteen analyses were conducted on 15 zircons (Table DR1). Among them, nine analyses showed variable levels of U and Th, from 277 ppm to 947 ppm and from 96 ppm to 614 ppm, respectively, with Th/U ratios between 0.26 and 0.98. These nine analyses have concordant U-Pb ages and show a tight group, yielding a weighted mean $^{206}\text{Pb}/^{238}\text{U}$ age of 460 ± 14 Ma (MSWD = 6.9), which is interpreted as the crystallization age of the Dabanxi intrusion (Fig. 7F). Two analyses (spot-4 and spot-6) give slightly older $^{206}\text{Pb}/^{238}\text{U}$ ages from 545 Ma to 514 Ma (Table DR1). Results from another four spots (spot-2, spot-8, spot-9, and spot-12) give younger $^{206}\text{Pb}/^{238}\text{U}$ ages from 423 Ma to 296 Ma, with higher common Pb than the others, suggesting that the U-Pb isotopic system might have been modified during postemplacement alteration.

Mineral Chemical Compositions

Nineteen clinopyroxene grains from the Dawan gabbros have SiO_2 contents between 48.90 and 52.70 wt%, CaO between 22.04 and 25.02 wt%, TiO_2 between 0.15 and 1.07 wt%, FeO between 4.98 and 6.17 wt%, and Na_2O in the range of 0.26–0.84 wt%. Calculations using Minpet (version 2.02) indicated that the clinopyroxenes exhibit high Mg# (82–85). These clinopyroxenes are characterized by high Ca and low Ti, Al, and Na, and they plot in the diopside field in the Wo-En-Fs diagram (Fig. 8A), resembling clinopyroxenes from Alaskan-type complexes (Snoke et al., 1981; Helmy and El Mahallawi, 2003; Ye et al., 2015). Furthermore, they define a clear arc cumulate trend in the Al^{VI} versus TiO_2 diagram (Figs. 8B and 8C; after Loucks, 1990).

Thirty-seven clinopyroxene grains from the Dabanxi gabbros were analyzed for chemical compositions (Table DR3). They have relative high SiO_2 (50.56–54.29 wt%) and Al_2O_3 (2.85–6.87 wt%) contents, low MgO (14.58–18.03 wt%), CaO (12.84–14.24 wt%), and TiO_2 (0–0.25 wt%) contents, and Mg# ranging from 66 to 78. They plot in the field of augite in the Wo-En-Fs diagram (Fig. 8A) and show arc-related features according to their SiO_2 , Al_2O_3 , and TiO_2 contents (Figs. 8B and 8C).

Whole-Rock Elemental Geochemistry

Seven gabbro samples from the Dawan intrusion, 10 andesite samples from the lower Lapeiquan Formation, and 10 gabbro samples from the Dabanxi intrusion were collected for major- and trace-element analyses (Table 1). The concentrations of major oxides, described below in weight percent, were recalculated to 100% on a volatile-free base.

All studied samples have undergone varying degrees of alteration, consistent with the observed fluctuation in loss on ignition (LOI) values (1.27–6.66 wt%). Thus, evaluation is required to assess the effects of alteration on the chemical compositions of these samples. Zirconium is conventionally regarded as an immobile element during low- to medium-grade alteration in igneous rocks (e.g., Wood et al., 1979). Therefore, a number of elements with different geochemical behaviors (e.g., Rb, Sr, Ba, Nb, La, Y, Th, U, and Ti) were plotted against Zr to evaluate their mobility during alteration (e.g., Fan et al., 2013). High field strength elements (HFSEs; Nb, Th, and Y), rare earth elements (REEs), U, and siderophile elements (such as Ti) showed strong correlations with Zr. In contrast, some large ion lithophile elements (LILEs; Rb, Sr, and Ba) were scattered over the plots (figure not shown). Consequently, mobile elements such as Rb, Sr, and Ba, and Sr isotopic compositions cannot be used in the geochemical classification and petrogenetic discussion.

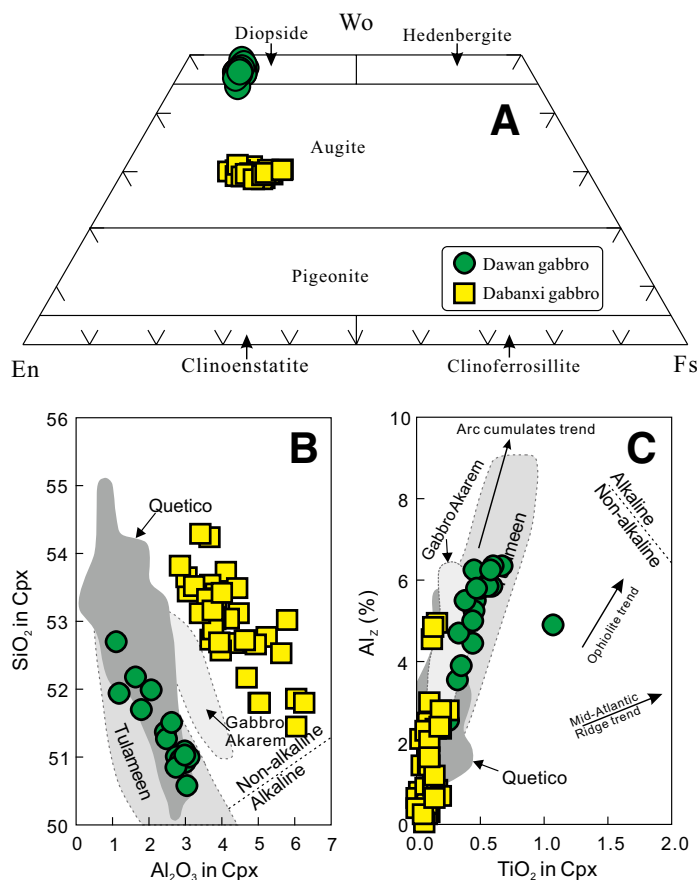
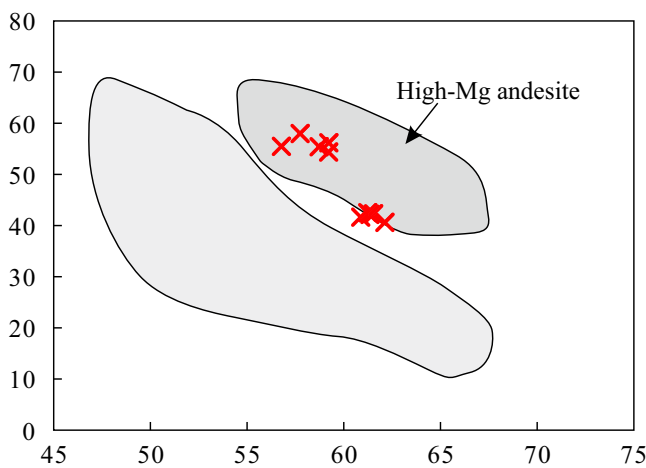
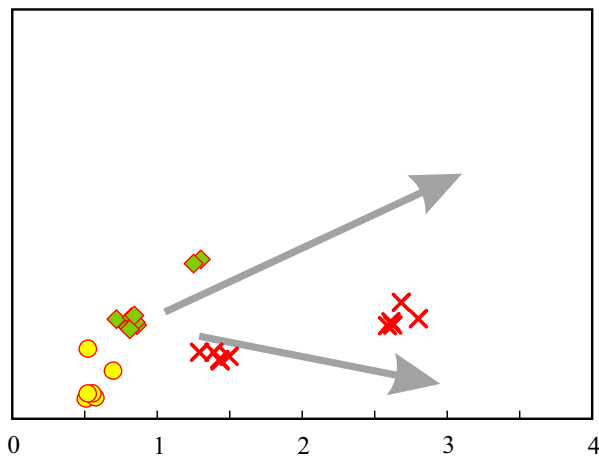
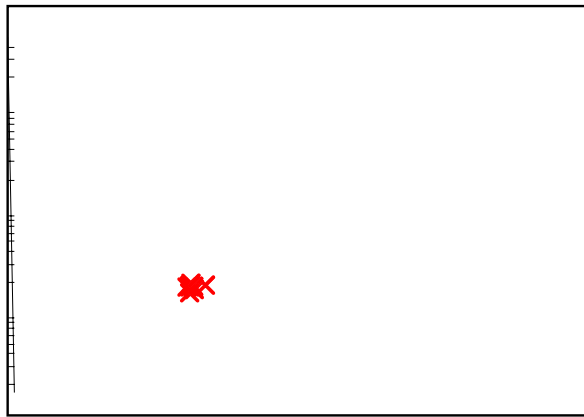


Figure 8. (A) Wo-En-Fs diagram showing the compositions of the clinopyroxene from the Dawan intrusion; (B) Al_2O_3 (wt%) vs. SiO_2 (wt%) and (C) TiO_2 (wt%) vs. Al^{IV} (percentage of tetrahedral site occupied by Al_2) in clinopyroxene from the Dawan intrusion. Gray fields are modified from Ye et al. (2015); reference lines of arc-related and rift-related tectonic environments are from Loucks (1990).

Dawan Intrusion

Gabbros from the Dawan intrusion have SiO_2 contents ranging from 47.2 to 51.9 wt% and display variable levels of $\text{Fe}_2\text{O}_3^{\text{T}}$ (4.54–7.52 wt%), Al_2O_3 (16.1–20.5 wt%), CaO (11.3–16.9 wt%), TiO_2 (0.21–0.71 wt%), Na_2O (1.22–2.24 wt%), and K_2O (0.11–1.02 wt%), owing to crystal fractionation/cumulation effects (Table 1). The gabbro samples plot in the subalkaline field of the total alkali-silica (TAS) diagram (figure not shown) and define a typical tholeiitic trend in the TiO_2 versus $\text{FeO}^{\text{total}}/\text{MgO}$ diagram (Fig. 9B).

The Dawan gabbros contain variable compatible element contents, e.g., Cr ranges from 334 to 1080 ppm, Ni ranges from 125 to 153 ppm, and V ranges from 104 to 209 ppm, due to crystal fractionation/cumulation. On the other hand, they have low total REE contents between 7.0 and 24.3 ppm (Table 1). The gabbros mostly show flat chondrite-normalized REE patterns, with $(\text{La}/\text{Yb})_{\text{N}}$ ranging from 0.99 to 1.07 (Fig. 10A). Significant positive Eu anomalies ($\delta\text{Eu} = 1.5\text{--}1.9$) are observed in several samples (AYT002H1, AYT002H3, AYT002H5, AYT002H7), yet another two (AYT002H2 and AYT002H6) show no obvious Eu anomalies ($\delta\text{Eu} = 0.99\text{--}1.07$; Fig. 10A). Normalized to primitive mantle, all samples exhibit variable enrichments in LILEs and pronounced Nb depletion ($\text{Nb}/\text{La} = 0.13\text{--}0.80$; Fig. 10B). The positive Sr anomalies are concurrent with the positive Eu anomalies, indicating plagioclase accumulation.



Dawan High-Mg Andesite

Andesite samples display varied levels of SiO₂ (56.8–62.1 wt%), Al₂O₃ (13.9–15.8 wt%), Fe₂O₃ (9.04–11.5 wt%), MgO (3.35–6.30 wt%), TiO₂ (0.61–1.21 wt%), and total alkali (Na₂O + K₂O = 1.52–4.02 wt%). These rocks plot in the field of andesite on the Zr–Ti–Nb–Y diagram (Fig. 9A; Winchester and Floyd, 1977), and they exhibit calc-alkaline trends in the TiO₂–FeO^{total}/MgO diagram (Fig. 9B). Furthermore, they can be classified as high-Mg andesite based on the Mg#–SiO₂ diagram (Fig. 9C).

Despite the observed variation in their REE abundances, all andesite samples display coherent REE patterns (Σ REE = 54.7–114 ppm). Chondrite-normalized REE patterns are markedly LREE-enriched (Fig. 10C), with (La/Yb)_N values ranging from 3.04 to 3.84. They also display significant negative Eu anomalies (δ Eu = 0.57–0.90) and relatively flat heavy (H) REE patterns (normalized [Gd/Yb]_N = 1.0–1.1; Table 1; Fig. 10C). Normalized to primitive mantle, all samples show variable degrees of depletion in HFSEs, such as Nb (Fig. 10D), thereby sharing an arc-related signature.

Dabanxi Intrusion

Gabbros from the Dabanxi intrusion have SiO₂ contents varying from 46.1 to 48.7 wt%, with relatively high MgO (8.53–12.0 wt%), Al₂O₃ (15.7–19.1 wt%), and TiO₂ (0.90–1.59 wt%) contents, but relatively low levels of total alkalis (Na₂O + K₂O = 2.11–2.98 wt%; Table 1). All samples plot in the subalkaline fields of the TAS diagram (figure not shown) and follow a typical tholeiitic trend in the TiO₂ versus FeO^{total}/MgO diagram (Fig. 9B).

The analyzed gabbros have varied levels of Cr (272–367 ppm), Ni (95–206 ppm), and V (167–260 ppm), with low total REE abundances (30–51 ppm). Chondrite-normalized patterns exhibit slight enrichment of LREEs ([La/Yb]_N = 1.53–1.78) and flat HREE ([Gd/Yb]_N = 1.28–1.42) patterns, with variably positive Eu anomalies (δ Eu = 1.11–1.31; Fig. 10E). On the primitive mantle–normalized spider diagrams, the gabbros are extremely depleted in Nb, with Nb/La ratios between 0.43 and 0.55, and variably enriched in Sr and Ba relative to their adjacent elements (Fig. 10F), resembling typical continental arc basaltic rocks (Rudnick and Gao, 2003).

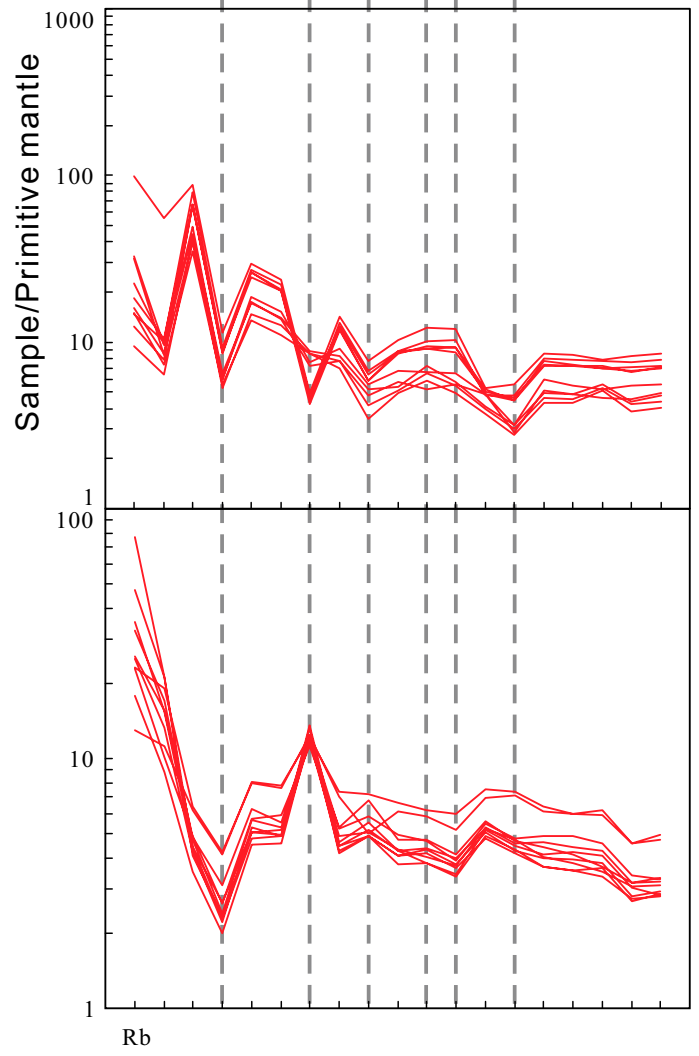
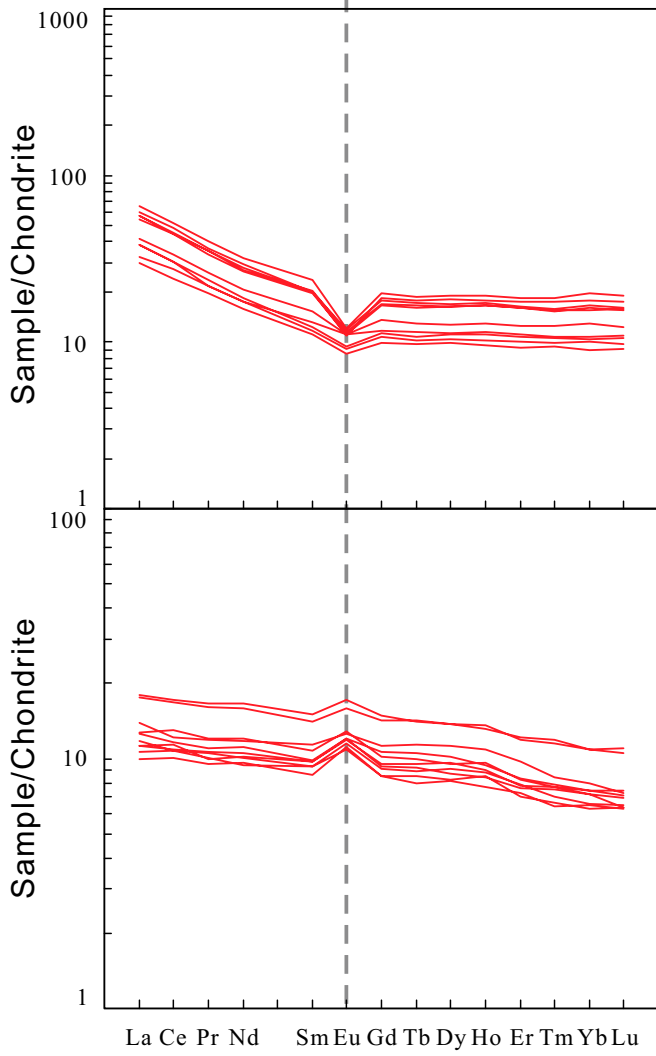
Whole-Rock Sr–Nd Isotopic Compositions

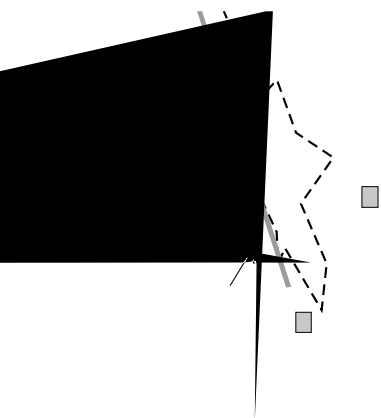
Dawan gabbros have varying ¹⁴⁷Sm/¹⁴⁴Nd ratios between 0.2065 and 0.2342, and ¹⁴³Nd/¹⁴⁴Nd ratios between 0.512700 and 0.513141, which correspond to a range of initial epsilon Nd ($t = 515$ Ma) values from +0.6 to +7.4 (Fig. 11). They also show highly varied ⁸⁷Rb/⁸⁶Sr ratios between 0.0385 and 0.3460 and a relatively large range of ⁸⁷Sr/⁸⁶Sr ratios from 0.7056 to 0.7078, corresponding to initial (⁸⁷Sr/⁸⁶Sr)_i ratios of 0.7046–0.7054 (Table 2). The samples from the Dabanxi intrusion show a narrow range of ⁸⁷Rb/⁸⁶Sr ratios (0.0932–0.1848) and ⁸⁷Sr/⁸⁶Sr ratios (0.7070–0.7080), as well as near-identical initial ⁸⁷Sr/⁸⁶Sr ratios (0.7059–0.7074). The neodymium isotopic compositions of samples from the Dabanxi intrusion have ¹⁴⁷Sm/¹⁴⁴Nd ratios between 0.1792 and 0.1890 and ¹⁴³Nd/¹⁴⁴Nd ratios between 0.512626 and 0.512825, with $\epsilon_{\text{Nd}}(t)$ values from +0.6 to +4.1 (Fig. 11). Positive $\epsilon_{\text{Nd}}(t)$ values and low (⁸⁷Sr/⁸⁶Sr)_i ratios suggest that the parental magmas of the Dawan and Dabanxi gabbroic intrusions were derived from depleted mantle sources. In contrast to the gabbros, the two representative andesite samples from the lower Lapeiquan Formation have nearly constant initial ⁸⁷Sr/⁸⁶Sr ratios (0.7117–0.7146) and negative $\epsilon_{\text{Nd}}(t)$ values in the range –3.7 to –5.8 (Fig. 11).

DISCUSSION

Depositional Age of the Lapeiquan Formation

As mentioned above, the ages of one rhyolitic sample from the lower Lapeiquan Formation and two rhyolite samples from the upper Lapeiquan





Formation indicated that the eruption of these volcanic rocks occurred over a short interval between 495 and 485 Ma, suggesting that this volcanoclastic-sedimentary sequence was deposited during the late Cambrian rather than Mesoproterozoic Era (Xinjiang BGMR, 1981) or Ordovician Period (Xinjiang BGMR, 2006). Moreover, previous geochronological studies demonstrated that granitic plutons that intruded the Lapeiquan Formation were mostly emplaced from 490 to 420 Ma, which is consistent with the age of deposition of the Lapeiquan Formation within analytical errors. Thus, we can conclude that the Lapeiquan Formation was deposited during the late Cambrian (495–485 Ma).

Petrogenesis

Dawan Gabbros

All selected gabbros from the Dawan intrusion are characterized by a strong depletion in Nb (Fig. 10B), indicating that a continental component might have been involved in their origin, as continental crust is typically depleted in Nb (Barth et al., 2000; Rudnick and Gao, 2003). Nevertheless, the following evidence argues against significant crust incorporation into the primitive magma: (1) There is no obvious correlation between Nb/La, U/Nb, or Th/La and SiO_2 for the Dawan gabbros (Figs. 12A, 12B, and 12C), which contradicts the contamination model because crustal material would diminish Nb/La ratios and elevate both U/Nb and Th/La ratios at the same time. (2) Crustal contamination could simultaneously elevate La/Sm ratios and decrease $\epsilon_{\text{Nd}}(t)$ values. However, no negative correlation between La/Sm and $\epsilon_{\text{Nd}}(t)$ has been observed (Fig. 12D). Thus, we conclude that no significant crustal contamination occurred in the formation of the Dawan gabbros.

Due to their notably depleted Nd isotopic compositions, the Dawan gabbros are comparable to normal mid-ocean-ridge basalt (N-MORB) generated by decompression partial melting of anhydrous peridotites associated with depleted asthenospheric mantle (Hirose and Kushiro, 1993; Zindler and Hart, 1986). Furthermore, their relatively flat REE

patterns also argue against an origin from partial melting of an enriched mantle wedge formed by fluid metasomatism in subduction zones. In addition, their geochemical signatures are similar to those of the Hongliugou ophiolites (Figs. 10A and 10B; Gao et al., 2012; Yang et al., 2008). Therefore, we reason that the Dawan gabbros were derived from depleted asthenospheric mantle. Nevertheless, compared to normal MORB, the Dawan gabbros exhibit significant Nb depletion on the primitive mantle-normalized diagrams, and lower Nd isotopic ratios than MORB (Figs. 10B and 11). This implies that enriched lithospheric mantle participated in the formation of the Dawan gabbros (Tang et al., 2006).

It has been demonstrated that formation of enriched lithospheric mantle can be attributed to previous melts or fluid metasomatism in ancient subduction zones (Pearce et al., 2005). Generally, slab-derived fluids are enriched in LILEs (e.g., K, Rb) and depleted in HFSEs (e.g., Nb, Ta), whereas LREEs and Th are strongly incorporated into subducted oceanic slab-derived melts (Tatsumi and Eggins, 1995; Woodhead et al., 2001). The Dawan gabbros are depleted in HFSEs and show a relatively large range of U/Th ratios (0.4–4.0), as well as low and constant Th/Nb ratios (0.11–0.55). These results imply that the lithospheric mantle had been metasomatized by ancient slab-derived hydrous fluids (Hawkesworth et al., 1993; Pearce and Peate, 1995; Saunders et al., 1991; Stern, 2002).

The Dawan gabbros show variable Mg# (72–78) and compatible elemental concentrations (e.g., Cr = 334–1080 ppm), indicating the samples underwent various degrees of fractional crystallization. Increasing CaO and Al_2O_3 contents with increasing Mg# indicate the fractionation of clinopyroxene (e.g., Yang and Zhou, 2009; Zhu et al., 2010), which is in agreement with the positive correlation of Cr with Mg#. On incompatible elements spider diagrams, the Dawan gabbros show positive Sr anomalies (Fig. 10B), implying accumulation of plagioclase, which is consistent with their positive Eu anomalies in the REE patterns (Fig. 10A).

Dawan High-Mg Andesites

We employed Nb/La, U/Nb, and Th/La ratios as indicators to evaluate the effect of crustal contamination of mantle-derived magmas. There are near-horizontal correlation patterns in the diagrams of Nb/La- SiO_2 , U/Nb- SiO_2 , and Th/La- SiO_2 (Figs. 12A, 12B, and 12C), arguing against significant crustal contamination during magma ascent. Moreover, the $\epsilon_{\text{Nd}}(t)$ values do not show large variations in these samples, which provide further evidence that the magmas were not notably affected by crustal materials. Thus, the geochemical characteristics of the Dawan high-Mg andesites can be used to decipher their mantle sources and the processes of their magma evolution.

Several magmatic processes has been proposed to explain the formation of high-Mg andesites, including (1) partial melting of hydrated peridotite (Kelemen, 1995; Straub et al., 2011; Tatsumi, 1981; Wood and Turner, 2009), (2) interaction between the lower crust and asthenosphere via delamination or slab breakoff (Xu et al., 2002; Gao et al., 2004; Q. Wang et al., 2006), (3) crustal-level magma mixing between crust-derived felsic and mantle-derived mafic magmas (Shellnutt and Zellmer, 2010; Streck et al., 2007), or (4) interaction between melts (slab and/or sediment) and the mantle wedge (e.g., Kelemen, 1995; X.W. Li et al., 2013; Qian et al., 2017; Tatsumi, 2001; Tsuchiya et al., 2005; Wang et al., 2011; Yagodinski et al., 1995).

High-pressure melting experiments have illustrated that partial melting of dry refractory peridotite cannot produce a high-Mg melt (Falloon et al., 1997), while hydrous peridotite can generate high-Mg andesitic melts with relatively low levels of TiO_2 (0.55–0.70 wt%), $\text{Fe}_2\text{O}_3^{\text{T}}$ (4.04–5.36 wt%), and Na_2O (1.10–3.09 wt%), as well as high concentrations of Al_2O_3 (17.2–21.7 wt%) and CaO (8.53–9.99 wt%; Hirose, 1997). However, the major oxides and negative Nd isotopic compositions of the Dawan

high-Mg andesites readily rule out the first model. Instead, andesitic melts, which are genetically related to the foundering of mafic lower crust into the underlying asthenospheric mantle followed by immediate partial melting, will produce the depleted signatures (Gao et al., 2004; Qin et al., 2010). Furthermore, partial melting of lower crust generates high-Mg adakitic magma with high Sr (>400 ppm) and Sr/Y (>20), low Y (<18 ppm) and Yb (<1.9 ppm), and high LREE/HREE ratios with (La/Yb)_N > 20 (e.g., X.R. Wang et al., 2006; Tang and Wang, 2010;7 (W)80 (ang, 205n;)68lu0ah81to1m6 Tw 0 -1.222 g et al.8(201H.5 (lo)25 (lov)1n)06 (80,

andesites were likely generated by interaction between sediment-derived melts and basaltic melts originating from mantle wedge peridotites.

Dabanxi Intrusion

The Dabanxi gabbroic rocks show significant Nb depletion on primitive mantle-normalized diagrams, and all samples exhibit slight LREE enrichment, implying possible involvement of a continental component in their origin. Nevertheless, the following evidence rules out the possibility of significant crustal component involvement in their origin: (1) The analyzed samples show a wide range of SiO₂ contents but relatively constant Nb/La (0.43–0.55), U/Nb (0.10–0.15), and Th/La (0.10–0.11) ratios (Figs. 12A, 12B, and 12C); (2) crustal contamination could simultaneously elevate La/Sm ratios and decrease ε_{Nd}(t) values; however, such a trend was not observed in the samples (Fig. 12D); and (3) no xenocrystic zircon indicative of crustal contamination was detected by CL imaging and SHRIMP zircon U-Pb dating.

Thus, we conclude that the parent magma of the Dabanxi intrusion reflects metasomatism of the mantle source, rather than crustal contamination. The large variation in Nd isotopic compositions might have resulted from the heterogeneity of the mantle source. In the Th/Nb versus U/Th diagram (Fig. 13), the Dabanxi gabbros show a wide distribution of U/Th ratios (0.48–0.71) with a narrow range of relatively low Th/Nb ratios (0.18–0.24), from the Dabanxi

These studies have identified two ophiolite zones (Hongliugou-Lapeiquan and south Altun) in the Altun orogenic belt and have demonstrated the existence of the North and South Altun Oceans (L. Liu et al., 1997, 2012). It is considered that the North Altun Ocean basin opened ca. 750 Ma (H. Liu et al., 2012) and then started to subduct from 520 to 500 Ma (Han et al., 2012; Kang et al., 2011; C. Liu et al., 2016; Wu et al., 2009), and then the subduction angle changed (e.g., slab rollback and flat-slab subduction) during 520–460 Ma, and it was completely closed by ca. 450 Ma (Hao et al., 2006). The existence of volcanic-arc granites on both sides of the Hongliugou-Lapeiquan ophiolite belt suggests that the oceanic lithosphere might have undergone divergent double-sided subduction (C. Liu et al., 2016; J.H. Liu et al., 2017). However, the petrogenesis of the Dawan gabbros and the Dawan high-Mg andesites cannot be sufficiently explained by a normal oceanic subduction event. These rocks were generally related to upwelling of asthenospheric mantle. Three competing mechanisms should be taken into account: (1) ocean-ridge subduction (e.g., Cai et al., 2012; Dickinson and Snyder, 1979; Windley et al., 2007; Sun et al., 2009; Zhang et al., 2014), (2) slab breakoff (e.g., Atherton and Ghani, 2002; Davies and von Blanckenburg, 1995; Niu et al., 2006; van Hunen and Allen, 2011), and (3) slab rollback (Hawkins et al., 1990; Xu et al., 2003; Yan et al., 2016).

Ocean-ridge subduction causes voluminous magmatic activity and HT/LP metamorphism (Kusky et al., 2003; Sisson et al., 2003; Windley et al., 2007). Ridge subduction is responsible for the formation of a slab window, which induces upwelling of hot and depleted asthenospheric mantle. This process generally accounts for the origination of MORB-like adakitic and boninitic rocks (Sisson et al., 2003). Recent studies indicate that the circum-Pacific regions have been affected by ridge subduction in the formation of the accretionary orogens in Japan, Alaska, and Chile (Cai et al., 2012, and references therein). Also, ridge subduction has been invoked in several regions of the Central Asian orogenic belt (e.g., West Junggar, Chinese Altai, and Inner Mongolia; Cai et al., 2012; Geng et al., 2009; Sun et al., 2009). However, the lack of coeval adakites and boninites in the North Altun clearly contradicts the ocean-ridge subduction model. Furthermore, there is no evidence for any high-temperature metamorphic events in this tectonic belt. These findings prompted us to rule out the possibility of ridge subduction during the Cambrian.

Slab breakoff associated with the final detachment of a lithospheric slab (Davies and von Blanckenburg, 1995; Xu et al., 2008) has been proposed as an explanation of the distinct igneous activity during the early stages of continent-continent or continent-arc collision (Atherton and Ghani, 2002; Davies and von Blanckenburg, 1995; Teng et al., 2000; Zhu et al., 2015). However, there is no evidence suggesting the occurrence of early Cambrian (ca. 520 Ma) collision in the North Altun. Instead, the subduction process most likely lasted until ca. 460 Ma in this area (Chen et al., 2016; Cui et al., 2010; Han et al., 2012; S.B. Li et al., 2013; Wu et al., 2016). Thus, the slab breakoff model cannot satisfactorily describe the origin of the Dawan gabbros and the Dawan high-Mg andesites.

Alternatively, it has been suggested that slab rollback played a key role in the generation of these temporally and spatially related igneous rocks. Rollback of the subducting slab would result in extension of the arc lithosphere (Gueguen et al., 1997), which is an important driving force of back-arc basin formation (Nakakuki and Mura, 2013). Partial melting of the upwelling asthenospheric mantle beneath an ocean-ridge system in a suprasubduction zone induces the formation of back-arc basin basalts, most of which show volcanic arc-like and MORB-like compositional characteristics (Evans et al., 1991; Hawkins et al., 1990; Xu et al., 2003).

The Dawan gabbros show varying extents of depletion or enrichment of LREEs and have high $\varepsilon_{\text{Nd}}(t)$ values, indicating that a component from depleted asthenospheric mantle was involved in their generation. However, all these gabbros plot between the MORB array and the field of arc-like

volcanics (Fig. 14A). Furthermore, the clinopyroxenes from the Dawan gabbros exhibit arc-related trends and plot in the overlapping area between normal MORB and back-arc basin basalt (Figs. 8C and 14B). These observations strongly argue that the Dawan gabbros share a systematic back-arc basin basalt compositional signature and that they were most probably formed in a back-arc basin environment, in apparent consistency with the slab rollback model. In this scenario, the migration of the subducting slab backward into the asthenospheric mantle (rollback) results in the upwelling and decompression melting of hot asthenospheric mantle. This process is followed by partial melting of the subcontinental lithospheric mantle, which ultimately leads to the formation of the parental Dawan gabbro melt. Asthenospheric upwelling results in high-temperature conditions that reheat the cooled subducted slab, subsequently causing sediment melting. These sediment-derived melts react with the mantle wedge and result in partial melting of the metasomatized mantle peridotites, generating magmas like the Dawan high-Mg andesite magmas. Thus, we argue that the slab rollback (formation of back-arc basin) model is also consistent with the formation of the slightly younger Dawan high-Mg andesites.

Previous studies have provided abundant evidence in support of the hypothesis that the North Altun is the western extension of the North Qilian, separated into two parts by the Altyn Tagh fault. Based on identification of a HP/LT metamorphic belt, ophiolites, a subduction-accretion complex, and arc magmatic rocks, the North Altun is considered to be an early Paleozoic accretionary orogen, recognized as the northernmost orogenic collage of the proto-Tethyan domain (Li et al., 2017; Zhang et al., 2015, 2017). The initial rifting of the North Altun Ocean (proto-Tethys) began around ca. 750 Ma, according to the ages of bimodal volcanics identified in the North Altun (H. Liu et al., 2012). Though the exact timing of the initial subduction is unknown, the ocean basin already existed during the early–late Cambrian, as indicated by the ages of the gabbro (480 Ma; Yang et al., 2008) and of the plagiogranite (518–512 Ma; Gai et al., 2015; Gao et al., 2012) from the Hongliugou ophiolitic mélange. From ca. 520 to 495 Ma, oceanic slab rollback induced back-arc extension and resulted in upwelling of the asthenospheric mantle. Dawan gabbro magmas and Dawan high-Mg andesites were generated at the back-arc and the forearc, respectively (Fig. 15A). From the late Cambrian (490 Ma) to the Middle Ordovician (460 Ma), during the subduction of the North Altun Ocean, hydrous fluids released from the slab metasomatized the refractory mantle wedge. The addition of water caused the mantle wedge to be partially melted. Basaltic underplating provided the heat necessary for the melting of the lower and middle crust, which was followed by the generation of arc-related voluminous felsic magmas in the North Altun (Fig. 15B; e.g., Chen et al., 2016; Cui et al., 2010; Han et al., 2012; S.B. Li et al., 2013; Wu et al., 2016).

CONCLUSIONS

(1) Zircon U-Pb dating from rhyolite interbedded in the Lapeiquan Formation shows that the Lapeiquan volcanic-sedimentary sequence was deposited during the late Cambrian (495–485 Ma).

(2) The Dawan gabbro melts were generated from the asthenosphere with variable degrees of contribution from the lithospheric mantle. Dawan high-Mg andesites originated from the subsequent interaction between sediment-derived melts and mantle wedge peridotites. The Dabanxi gabbros were derived from the mantle wedge, which was metasomatized by fluids released from the subducted slab.

(3) The slab rollback model provides a satisfactory explanation of how the Dawan gabbros and the Dawan high-Mg andesites were formed in the North Altun, as the subduction of the North Altun Ocean might have lasted until ca. 460 Ma.

ACKNOWLEDGMENTS

We thank Dr. [Name] for providing the [Name] and [Name] antibodies. We also thank Dr. [Name] for providing the [Name] antibody. This work was supported by the [Name] and the [Name].

REFERENCES CITED

[Author], [Year]. [Title]. [Journal]. [Volume], [Page].

The first part of the paper describes the general geology of the study area, including the distribution of the main rock types and the structural features. The latter part of the paper is devoted to the detailed description of the deformation zones, their orientation, and their kinematics. The data obtained from the field observations are compared with the results of the laboratory experiments performed on samples collected from the study area. The results of the laboratory experiments show that the deformation zones in the study area are formed by the same mechanisms as those observed in the laboratory. The deformation zones are characterized by a high degree of localization of the strain, and they are formed by the same mechanisms as those observed in the laboratory. The data obtained from the field observations and the laboratory experiments are used to construct a structural map of the study area, which shows the distribution of the main rock types and the structural features.

The results of the field observations and the laboratory experiments show that the deformation zones in the study area are formed by the same mechanisms as those observed in the laboratory. The deformation zones are characterized by a high degree of localization of the strain, and they are formed by the same mechanisms as those observed in the laboratory. The data obtained from the field observations and the laboratory experiments are used to construct a structural map of the study area, which shows the distribution of the main rock types and the structural features. The results of the field observations and the laboratory experiments are compared with the results of the laboratory experiments performed on samples collected from the study area. The data obtained from the field observations and the laboratory experiments are used to construct a structural map of the study area, which shows the distribution of the main rock types and the structural features.

The first part of the paper discusses the importance of the research and the objectives of the study. It highlights the need for a comprehensive understanding of the subject matter and the role of the researcher in this process. The second part of the paper describes the methodology used in the study, including the data collection methods and the analysis techniques. The third part of the paper presents the results of the study, which show a significant correlation between the variables being studied. The fourth part of the paper discusses the implications of the findings and the potential applications of the research. The final part of the paper concludes the study and provides a summary of the key findings.

The second part of the paper discusses the methodology used in the study, including the data collection methods and the analysis techniques. The third part of the paper presents the results of the study, which show a significant correlation between the variables being studied. The fourth part of the paper discusses the implications of the findings and the potential applications of the research. The final part of the paper concludes the study and provides a summary of the key findings.

A SC, C 6 B A, 2018
 S A SC, C 20, 2018
 A SC, ACC, 6 S, B 2018